catalysts

MDPI

Article

Influence of Synthesis Conditions on Physicochemical and Photocatalytic Properties of Ag Containing Nanomaterials

Salwa D. Al-Malwi, Rahmah H. Al-Ammari, Abdulmohsen Alshehri and Katabathini Narasimharao *

Chemistry Department, Faculty of Science, King Abdulaziz University, P.O. Box 80203, Jeddah 21589, Saudi Arabia

* Correspondence: nkatabathini@kau.edu.sa; Tel.: +966-538638994

Abstract: Silver (Ag) containing nanomaterials were successfully prepared by varying synthesis conditions to understand the influence of preparation conditions on the physicochemical and photocatalytic properties of these materials. Different analytical techniques such as X-ray diffraction (XRD), Fourier transform infrared spectroscopy (FT-IR), Scanning electron microscopy (SEM), Diffuse reflectance UV-*vis* spectra (DR UV-*vis*), X-ray photoelectron spectroscopy (XPS) measurements, and N_2-physisorption were used to investigate the physicochemical properties of synthesized Ag containing nanomaterials. The samples (Ag-1 and Ag-2) prepared using $AgNO_3$, $NaHCO_3$, and polyvinylpyrrolidone (PVP) template exhibited pure Ag metal nanorods and nanoparticles; the morphology of Ag metal is influenced by the hydrothermal treatment. The Ag-3 sample prepared without PVP template and calcined at 250 °C showed the presence of a pure Ag_2O phase. However, the same sample dried at 50 °C (Ag-4) showed the presence of a pure Ag_2CO_3 phase. Interestingly, subjecting the sample to hydrothermal treatment (Ag-5) has not resulted in any change in crystal structure, but particle size was increased. All the synthesized Ag containing nanomaterials were used as photocatalysts for *p*-nitrophenol (*p*-NP) degradation under visible light irradiation. The Ag-4 sample (pure Ag_2CO_3 with small crystallite size) exhibited high photocatalytic activity (86% efficiency at pH 10, *p*-NP concentration of 16 mg L^{-1}, 120 min and catalyst mass of 100 mg) compared to the other synthesized Ag containing nanomaterials. The high photocatalytic activity of the Ag-4 sample is possibly due to the presence of a pure Ag_2CO_3 crystal structure with nanorod morphology with a low band gap energy of 1.96 eV and relative high surface area.

Keywords: silver nanomaterials; synthesis conditions; photodegradation; *p*-nitrophenol; visible light

Citation: Al-Malwi, S.D.; Al-Ammari, R.H.; Alshehri, A.; Narasimharao, K. Influence of Synthesis Conditions on Physicochemical and Photocatalytic Properties of Ag Containing Nanomaterials. *Catalysts* **2022**, *12*, 1226. https://doi.org/10.3390/catal12101226

Academic Editor: Roberto Comparelli

Received: 16 September 2022
Accepted: 10 October 2022
Published: 13 October 2022

1. Introduction

At present, the world is facing enormous challenges in finding clean drinking water, as many countries in the world are facing the problem of lack of healthy drinking water, especially under-developed and developing countries [1]. Water pollution can cause many problems in different sectors including public health, agricultural production, and industry, as well as on the country's economy [2]. Water pollution includes the pollution of water sources on the Earth, whether fresh water, seawater, or groundwater [3]. Water pollution by certain human activities enormously increased due to usage of agricultural fertilizers, pesticides, food processing waste, heavy metals, organic and inorganic pollutants, chemical waste, factory waste, etc. [4]. Inorganic and organic pollutants are the main contaminants in wastewater [5]. Organic and inorganic pollutants from chemical industry are carcinogenic, toxic, and non-biodegradable in nature [6]. Inorganic pollutants include some of heavy metals such as chromium (Cr), mercury (Hg), cadmium (Cd), lead (Pb), arsenic (As), etc., whereas organic pollutants include phenols, chlorinated phenols, azo dyes, polyaromatic hydrocarbons, polychlorinated biphenyls, polychlorinated dibenzofurans, etc. Nitrophenols [for instance *p*-nitrophenol (*p*-NP)] are carcinogenic and toxic compounds [7,8], which could cause disorder to the liver, kidneys, and blood of humans and animals and have been

classified as one of the most dangerous pollutants in many countries. However, it is still one of the most used pollutants in many products [8,9], such as pesticides, herbicides [10], paints and synthetic dyes [11], and pharmaceuticals [12]. The *p*-NP has been detected in natural water and wastewater due to its high solubility and water stability [13]. Therefore, it is very important to develop an efficient method to reduce the levels of *p*-NP in water to 10 ng/L as per the Environmental Protection Agency (EPA) standards [14].

The adsorption and coagulation techniques focuses on removal of contaminants in the water by transferring them to other stages, but the contaminants are still present in the water and are not eliminated [15]. Other methods also used in water treatment such as sedimentation, filtration, chemical, and membrane techniques can lead to toxic secondary pollutants and high operating costs [16]. Photocatalysis is recognized as one of the best methods used to degrade organic pollutants into harmless products such as water and carbon dioxide [17]. Most other methods are either multi step, expensive, or involve special instrumentation and produce toxic by-products. Photocatalytic technology has several advantages (including utilization of sunlight as renewable resource), the most important of which is complete mineralization and efficient removal of the organic pollutants, and simplistic operation procedures [18,19]. Li et al. [20,21] synthesized $Bi_2O_2CO_3$ nanostructures with different morphologies using different synthesis methods. The photocatalytic activities of nanomaterials were studied for photodegradation of MB and reduction of Cr(VI) ions under simulated-sunlight. The authors observed that nanoparticles of $Bi_2O_2CO_3$ exhibited high photocatalytic activity.

Silver (Ag)-based semiconductors are well-known photocatalysts with a distinctive response to visible light, and a high photocatalytic performance for the degradation of various organic contaminants, hence, these materials are considered as promising photocatalysts [22,23]. Various Ag-based materials such as $AgSbO_3$ [24], Ag_2CO_3 [25], Ag_3PO_4 [26], AgCl [27], Ag_3VO_4 [28], and Ag_2O [29] have been utilized for photocatalytic applications. It was previously reported that the characteristic properties such as crystalline structure, size, morphology, and surface area play a crucial role in photocatalysis [28]. Therefore, in this study, Ag based nanomaterials were successfully synthesized by adopting different synthesis conditions to investigate their influence on physicochemical and photocatalytic properties of the materials. Different analytical techniques such as XRD, FT-IR, SEM, DRUV-*vis*, N_2-physisorption, and XPS were used to investigate the physicochemical properties of synthesized Ag nanomaterials. In addition, the synthesized Ag nanomaterials were used as photocatalysts for degradation of *p*-NP under visible light irradiation. A correlation between the synthesis conditions, physicochemical properties, and photocatalytic activity of synthesized Ag containing nanomaterials was obtained.

2. Results and Discussion

2.1. XRD Analysis

The XRD patterns of synthesized samples are shown in Figure 1. All samples are highly crystalline and exhibited sharp diffraction peaks. The XRD patterns of Ag-1 and Ag-2 samples prepared with PVP-K36 template shown four major diffraction peaks at $2\theta = 38.16^\circ$, 44.26°, 64.51°, and 77.44° for Ag-1 and at $2\theta = 37.76^\circ$, 44.02°, 64.10°, and 77.11° for Ag-2 samples. All the diffraction peaks of Ag-1 and Ag-2 samples could be assigned to the (111), (200), (220), and (311) planes of the face-centered cubic (*fcc*) structure of silver metal (Ag^0) crystallites [JCPDS file 04-0783]. No other diffraction peaks are detected in both samples, indicating that the both Ag-1 and Ag-2 samples were composed of a pure Ag metal phase.

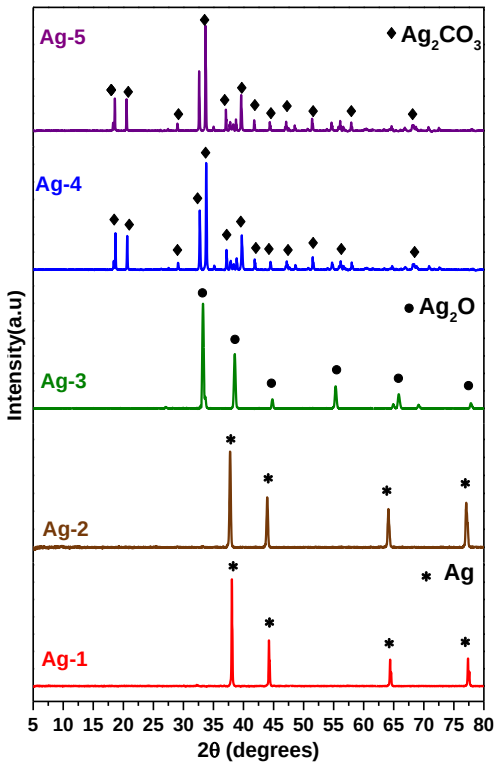

Figure 1. XRD patterns of synthesized Ag-containing nanomaterials.

The average crystal sizes of the Ag metal phase in Ag-1 and Ag-2 samples are 19.8 nm and 19.9 nm, respectively, as per the crystallite size calculated by the Scherrer equation (Equation (1)).

$$D = \frac{k\lambda}{\beta \cos\theta} \quad (1)$$

'D' is the crystal size, 'k' is the Scherer constant ($\simeq 0.9$), 'λ' is the X-ray wavelength (0.1546 nm), 'β' is the full width at half-maximum of the major XRD reflection in radians, and 'θ' is the Bragg angle. It is interesting to note that the average crystal size of Ag metal particles in the sample subjected to hydrothermal process is same as the crystallite size of the sample without hydrothermal process, which means that the hydrothermal treatment did not affect the crystallite size of Ag metal. The interaction mechanism of the silver nitrate, PVP template, and sodium bicarbonate and thermal decomposition under hydrothermal conditions to obtain nanosized Ag metal particles (Ag-1) without reducing agent is not very clear. However, it is generally assumed that because of the formation of crystals due to the poor thermal stability of silver carbonate precipitate, it easily decomposes into silver metal under hydrothermal conditions [30]. Equation (2) shows the chemical reaction of the whole process. As the reaction progresses, new silver atoms are gradually generated. When the concentration of these silver atoms reaches critical supersaturation, they will nucleate, and the formed silver crystal nuclei will grow to generate nanosized silver metal particles [31].

$$2Ag_2CO_3 \rightarrow 4Ag + 2CO_2 \uparrow + O_2 \uparrow \quad (2)$$

The PVP is known as a protective agent to prepare stable metal nanoparticles and it has a very good stabilizing effect on controlling the generation of nanoparticles of a certain size [32]. It is expected that the surface of the generated nanosized silver metal particles are covered by a large number of PVP molecules, thus preventing the formation multi-layers of Ag and preventing the agglomeration of Ag metal nanoparticles [32]. The Ag-2 sample, which was prepared without hydrothermal treatment, also yielded Ag metal particles, probably due to calcination of obtained product at 400 °C. The formed silver carbonate-PVP

composite was decomposed into Ag metal nanoparticles due to high temperature treatment. It was previously reported that PVP is widely used as a stabilizing and shape-directing agent in metallic NPs such as Ag, Au, and Cu [33]. The reported observations are consistent with the previous studies [34], which reported that the silver carbonate decomposed to silver oxides from 180 °C to 250 °C and the silver oxide decomposed into silver at above 300 °C (Equations (3) and (4)). In addition to the chemical decomposition of silver carbonate into silver metal at high temperatures, it is also possible that PVP influenced controlling the rate of reduction of silver ions [35].

$$Ag_2CO_3 \rightarrow Ag_2O + CO_2 \uparrow \quad (3)$$

$$2Ag_2O \rightarrow 4Ag + O_2 \uparrow \quad (4)$$

Figure 1 also shows the XRD pattern of the Ag-3 sample prepared without PVP and hydrothermal treatment. This sample exhibited the diffraction peaks at 2θ = 32.72°, 37.98°, 54.79°, 65.34°, and 68.59°, corresponding to the (111), (200), (220), (311), and (222) planes of cubic structure of Ag_2O [JCPDS file 76-1393]. Initially formed Ag_2CO_3 precipitate is transformed into Ag_2O phase due to thermal treatment at 250 °C as per Equation (4) and the average crystal size of Ag_2O is found to be 29.1 nm based on the calculation using the Scherrer equation. The XRD patterns of Ag-4 and Ag-5 samples (Figure 1) shows the diffraction peaks at 2θ = 18.81°, 20.60°, 29.22°, 32.71°, 33.77°, 37.35°, 39.79°, 41.90°, 44.59°, 47.27, 48.73°, 51.58°, 54.75°, 56.21°, and 58.08° were assigned to the (020), (110), (011), (-101), (-130), (200), (031), (220), (131), (230), (211), (150), (-231), (231), and (060) planes of the monoclinic Ag_2CO_3 structure [JCPDS file 26-0339]. The average crystallite sizes calculated from Shearer's equation for Ag-4 and Ag-5 samples are 45.3 nm and 49.4 nm, respectively. It is interesting to note that the sample which was subjected to hydrothermal treatment (Ag-5) possessed big size crystals compared to the sample without hydrothermal treatment. This is probably due to the difference in the morphology of the samples.

2.2. SEM Analysis

Scanning electron microscopy (SEM) is used to obtain information about the morphology of synthesized Ag-containing nanomaterials. From Figure 2, it can be observed that the Ag-1 sample prepared by hydrothermal process with PVP template showed nanowire morphology, while the sample prepared without hydrothermal treatment (Ag-2) exhibited irregular spherical particles. On the other hand, the Ag-3 sample shows the presence of near spherical morphology of Ag_2O with random particle distribution. The SEM images of Ag-4 and Ag-5 samples possessed tightly packed agglomerated rod-shaped particles with a smooth surface, as can be seen in Figure 2. The particle sizes in the samples measured from SEM analysis are compared with the crystallite sizes obtained using Shearer's equation (Table 1). Obviously, the particle sizes are higher compared to crystallite sizes due to fact that the particles are composed of several grains and the grain is constructed of combination of several crystallites.

Table 1. Data obtained from XRD, SEM, DR UV-*vis*, and N_2-physisorption analyses.

Sample	Crystallite Size (nm) a	Particle Size (nm) b	Band Gap (eV) c	Surface Area (m^2/g) d	Pore Volume (cc/g) d	Pore Radius (nm) d
Ag-1	19.8	30	2.46	29.9	0.029	2.45
Ag-2	19.9	40	2.45	42.5	0.039	2.45
Ag-3	29.1	42	2.29	46.0	0.045	2.84
Ag-4	45.3	58	1.96	56.4	0.053	2.84
Ag-5	49.4	75	2.17	48.5	0.049	2.84

a XRD, b SEM, c DR UV-*vis* spectroscopy, d N_2-physisorption.

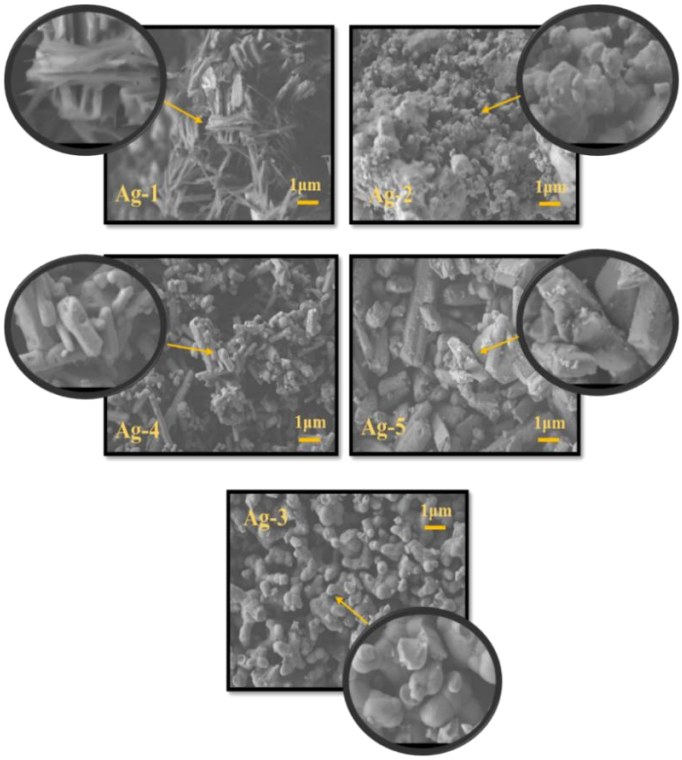

Figure 2. SEM images of synthesized Ag-containing nanomaterials.

2.3. FT–IR Analysis

The FT-IR spectra of all the synthesized samples are presented in Figure 3. The spectra of all the samples exhibited intense and broad IR absorption bands in the range of 3200–3550 cm^{-1} and 1648 cm^{-1} due to stretching and deformation vibrations of –OH groups of adsorbed water molecules [36]. The samples also exhibited bands at 680 cm^{-1}, 889 cm^{-1}, and 1412 cm^{-1}, which are characteristic bands for the CO_3^{-2} ions [37]. In addition, the bands appeared at 1061 cm^{-1}, 1687 cm^{-1}, and 590 cm^{-1} in the IR spectra of the samples, which could be assigned to stretching of the C-O group [38] and Ag–O vibration [38], respectively. These observations indicate that all the synthesized Ag containing nanomaterials have similar functionalities, however, the intensity of the peaks is different for the samples due to the number of functionals group presented in the samples being different. The Ag-4 and Ag-5 samples possessed a greater number of the –OH functional groups compared to the other synthesized samples.

2.4. DR UV–vis Spectroscopy

Figure 4 shows the DR UV–*vis* absorption spectra for all the synthesized samples. The Ag-1 and Ag-2 samples exhibited major UV light absorption peak at 320 nm, which could be assigned to strong surface plasmon resonance (SPR) of Ag metallic nanoparticles [39]. The less intense broad absorption peak in between 380–450 nm could be due to light absorption by the Ag oxide. It is well reported that Ag metal and Ag oxide nanoparticles exhibit SPR absorption peaks around 400 nm due to the combined vibration of electrons [40]. Fakhri et al. [41] studied the effect of annealing opto-electronic properties of Ag_2O films. The authors found that the incident light wavelength is directly related to the increase in the oxidation temperature and is caused by the transformation of metallic Ag to Ag_2O.

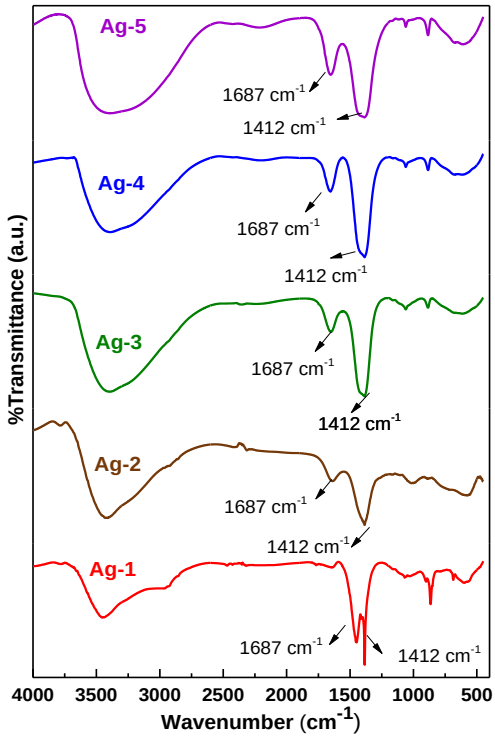

Figure 3. FT–IR spectra of synthesized Ag-containing nanomaterials.

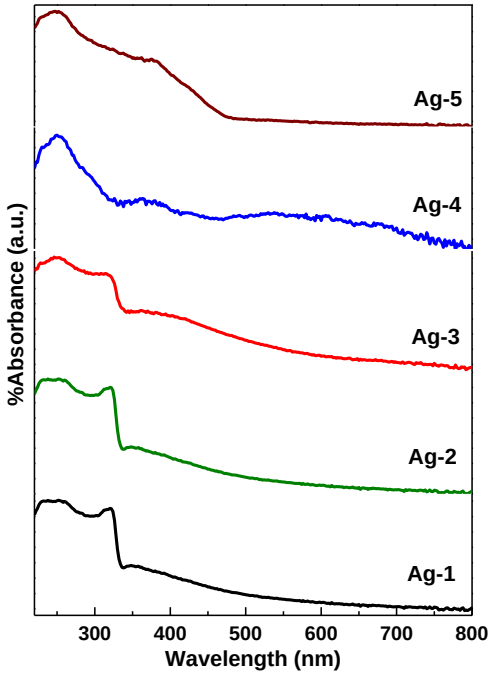

Figure 4. DR UV-vis spectra of synthesized Ag-containing nanomaterials.

The Ag-3 sample exhibited similar UV-*vis* absorption peaks as Ag-1 and Ag-2 samples, except that the intense broad absorption peak was observed in between 350–500 nm due to the light absorption by the Ag oxide. On other hand, the Ag-4 and Ag-5 samples, which are composed of silver carbonate, exhibited an intense broad peak centered at 400 nm. It was previously reported that Ag_2CO_3 powder could absorb solar energy with a wavelength shorter than 480 nm [42]. It is clear from Figure 4 that the visible edge is steep in Ag-4 and Ag-5 samples, indicating that the photoelectron transition from VB to CB is intrinsic due to the visible light absorption by the Ag_2CO_3 nanoparticles.

The Figure 5 shows Tauc plots for all the samples to measure the band gap energy (E_g). The band gap energy calculation of semiconductors is an important to know the ability of a semiconductor in photocatalysis application. The E_g was determined by using Equation (5).

$$\alpha hv = \left(Ahv - E_g\right)^n \quad (5)$$

where hv is the energy of photon ($1240/\lambda$), α is the linear absorption coefficient, and n is 2 for indirect transition. The function of Kubelka-Munk ($F(R)$) is proportional to α, therefore, Equation (5) becomes

$$F(R)hv = \left(Ahv - E_g\right)^n \quad (6)$$

The E_g for all the samples were determined from the Tauc plots. The band gap of the Ag-1 and Ag-2 samples is almost same (2.46 eV and 2.45 eV), while the Ag-3 sample possessed the band gap of 2.29 eV. It is well known that Ag metal nanoparticles should not have CB or VB. Although, both Ag-1 and Ag-2 samples were majorly composed of Ag metal phase, and the surface of the samples was oxidized to form silver oxide (XPS results). For this reason, the samples have CB and VB corresponding to silver oxide phase presented on the surface of the Ag-1 and Ag-2 samples. The lowest band gap values were observed for Ag-4 and Ag-5 samples: 1.96 eV and 2.17 eV, respectively. These results indicated that the Ag-4 and Ag-5 samples, which contained a silver carbonate phase, could exhibit high photocatalytic activity under visible light due to generation of more electron-hole pairs under visible light irradiation. Further, the valence band (VB) and conduction band (CB) potentials at the point of zero charge can be calculated using the band gap value, as seen in Equations (7) and (8)

$$E_{VB} = X - E_e + 0.5E_g \quad (7)$$

$$E_{CB} = E_{VB} - E_g \quad (8)$$

where X is the electronegativity of semiconductor and E_e is the free energy of electron on the hydrogen scale (4.5 eV). The electronegativity of Ag, Ag_2O, and Ag_2CO_3 is 1.93, 5.29, and 6.02, respectively. Scheme 1 shows CB and VB potentials for all the synthesized samples.

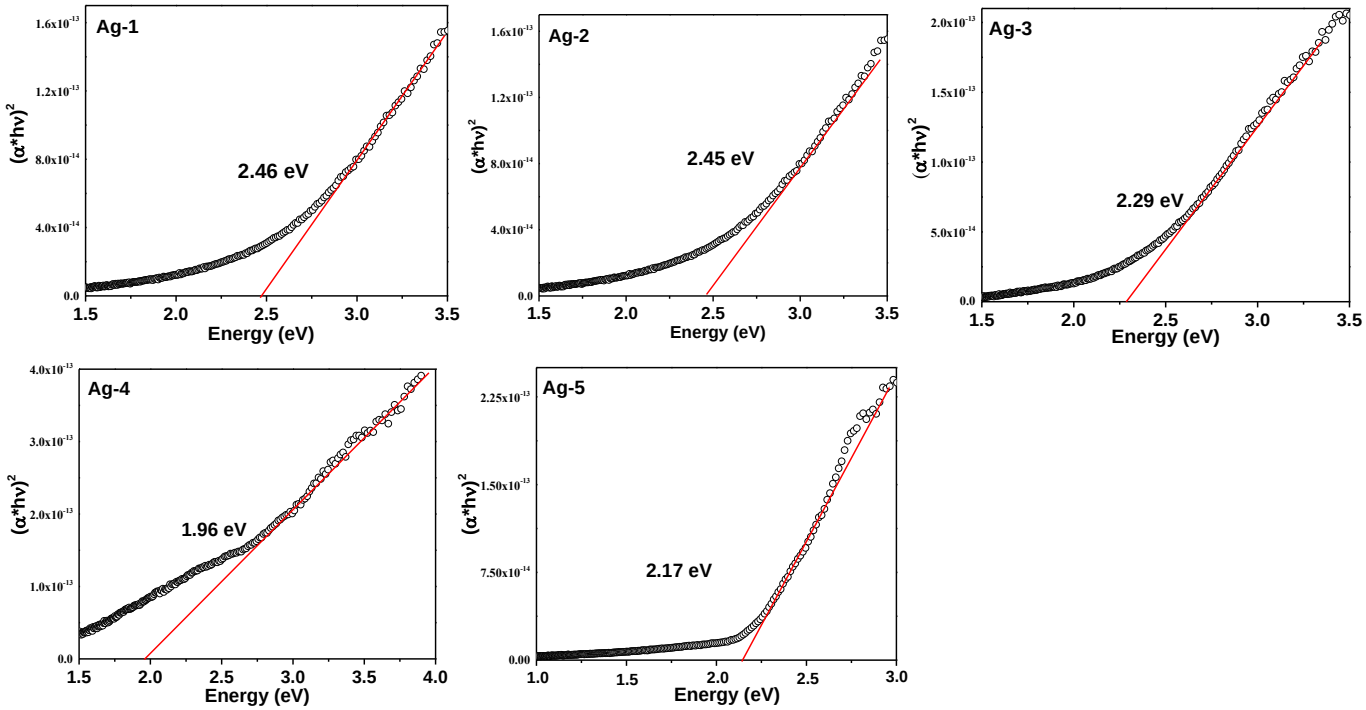

Figure 5. The Tauc plots for synthesized Ag-containing nanomaterials.

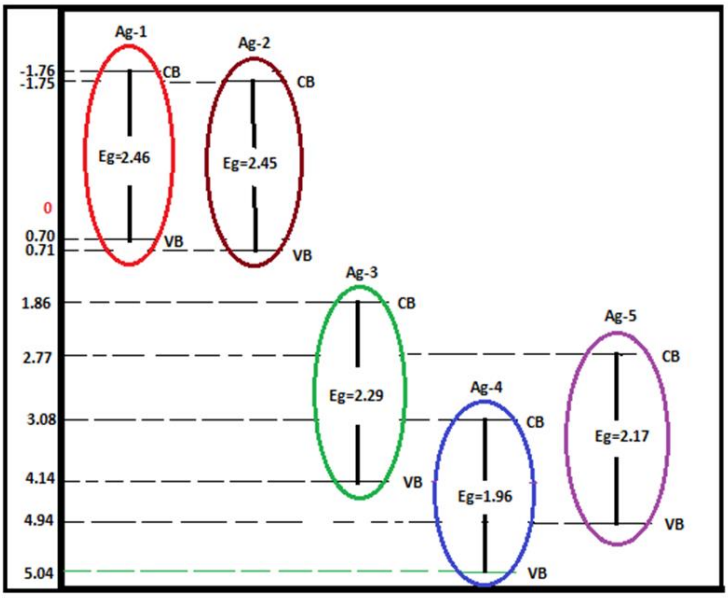

Scheme 1. Energies of CB and VB for synthesized Ag-containing nanomaterials.

2.5. XPS Analysis

To investigate the oxidation states of different elements and the surface chemical composition of the prepared samples, XPS analysis was performed (Figure 6). The deconvoluted Ag*3d* XPS spectra for all synthesized Ag containing samples showed a major doublet at 367.7 eV and 373.8 eV, and minor doublet at 374.8 eV and 368.6 eV, corresponding to $Ag3d_{5/2}$ and $Ag3d_{3/2}$ components of Ag^+ and Ag^0 species, respectively [43], confirming that all the samples contained both surface Ag^0 and Ag^+ species. Presence of a greater number of surface Ag^+ species compared to metallic Ag species in both Ag-1 and Ag-2 samples is probably due to surface Ag^0 transformation to Ag_2O. Interestingly, presence of surface Ag^0 species in Ag-4 and Ag-5 samples is due to decomposition of silver carbonate into silver above 300 °C [44].

The Ag-1 sample showed two deconvoluted O*1s* peaks at 530.7 eV and 531.3 eV. On the other hand, Ag-2 and Ag-3 samples showed three deconvoluted O*1s* peaks at 531.1 eV, 532.7 eV, and 535.6 eV and 530.7 eV, 532.0 eV, and 533.4 eV, respectively. The O*1s* peaks positioned in the range of 530–532 eV could be attributed to lattice oxygen, while the peak in the range of 532.2–533.5 eV and in the range of 533.5–536 eV corresponding to the oxygen species present in the surface absorbed the oxygen species and surface hydroxyl groups, respectively [44]. The presence of lattice oxygen in Ag-1 and Ag-2 samples indicates the presence of silver oxide, which was covered on the surface of silver metal nanoparticles.

The O*1s* spectra of Ag-4 and Ag-5 samples also exhibited two peaks at binding energies of 530.8 eV and 531.2 eV, corresponding to lattice oxygen of silver carbonate and in OH^- or H_2O species, respectively [45]. It can be clearly seen that the Ag-4, and Ag-5 samples (Ag_2CO_3) showed additional C*1s* species. The C*1s* spectrum of Ag-4 sample deconvoluted into four peaks at 288.7 eV, 288.1 eV, 284.6 eV, and 284.9 eV, while the C *1s* spectrum of the Ag-5 sample showed similar peaks, however, with a small shift at 288.6 eV, 287.4 eV, 284.5, eV, and 286.4 eV, and these peaks could be assigned to aliphatic C-C [46], C=O [47], and C-O-C [48] functional groups, respectively. The observed results clearly indicate the structural and electronic differences between the synthesized Ag-containing nanomaterials.

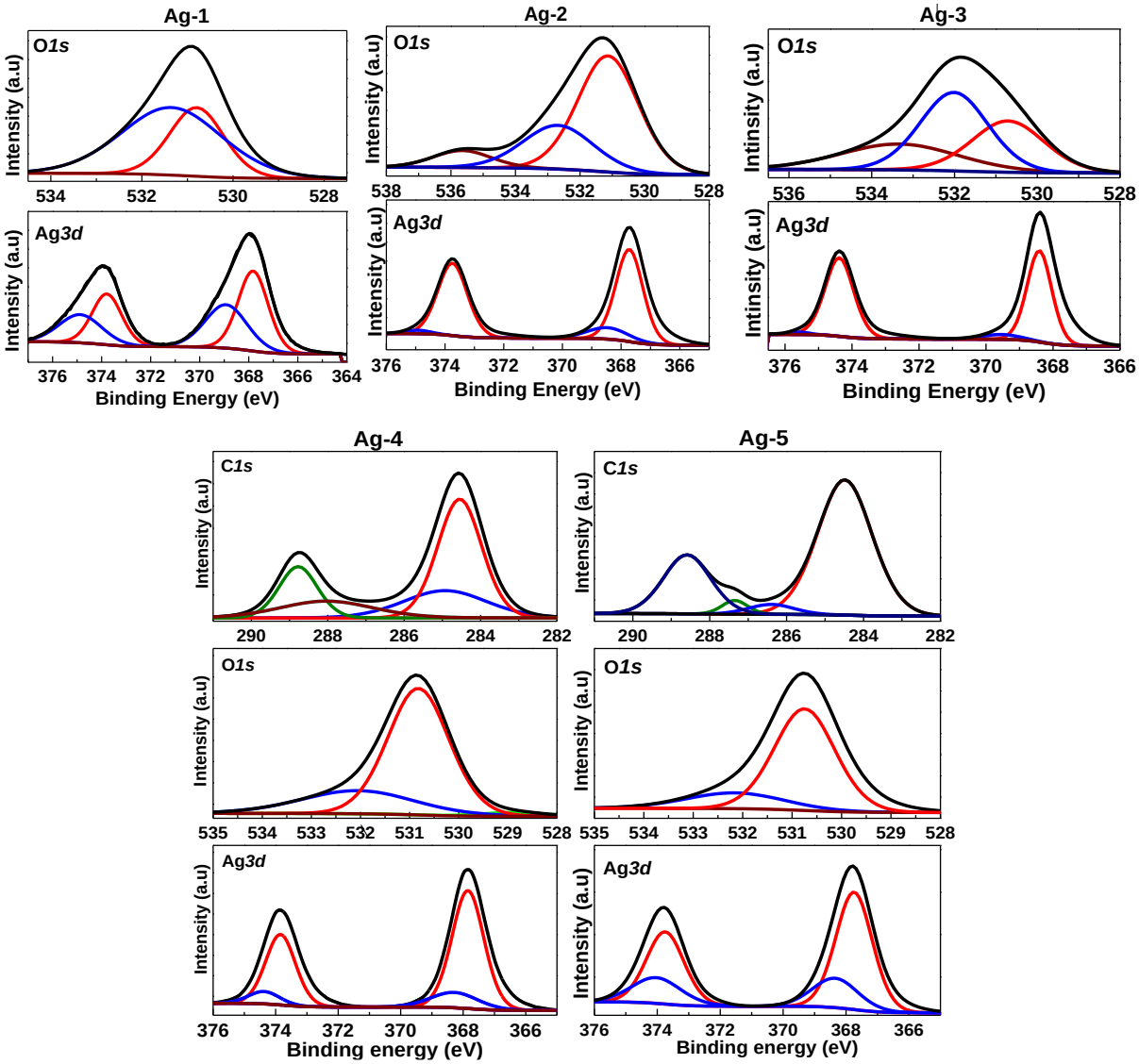

Figure 6. Deconvoluted XPS spectra for synthesized Ag-containing nanomaterials.

2.6. N_2-Physisorption Measurements

The data from N_2-physisorption experiments provide information about the textural properties of the samples such as surface area, pore volume, and pore radius. Figure 7 shows the N_2 adsorption-desorption isotherms and pore size distribution patterns (inset) of the samples. All the synthesized samples (Ag-1, Ag-2, Ag-3, Ag-4, and Ag-5) showed a type IV adsorption–desorption isotherm with an H3-type hysteresis loop, which reveals that the samples possess mesopores with a wide distribution of pore size as per IUPAC classification [49].

The pore size distribution patterns indicated that both Ag-1 and Ag-2 samples have pores with a radius of 2.45 nm, while it is 2.84 nm for Ag-3, Ag-4, and Ag-5 samples. The formation of mesopores is probably due to the aggregation of silver metal nanoparticles in Ag-1 and Ag-2 samples as shown in the SEM analysis, while the Ag-3, Ag-4, and Ag-5 samples were majorly composed of Ag oxide and carbonates. The BET surface area is calculated as 29.9, 42.5, 46.0, 56.4, and 48.6 m^2/g for Ag-1, Ag-2, Ag-3, Ag-4, and Ag-5, respectively (Table 1). The Ag-4 and Ag-5 samples possessed a high surface area and pore volume, probably due to the presence of silver carbonate nanorods in these samples.

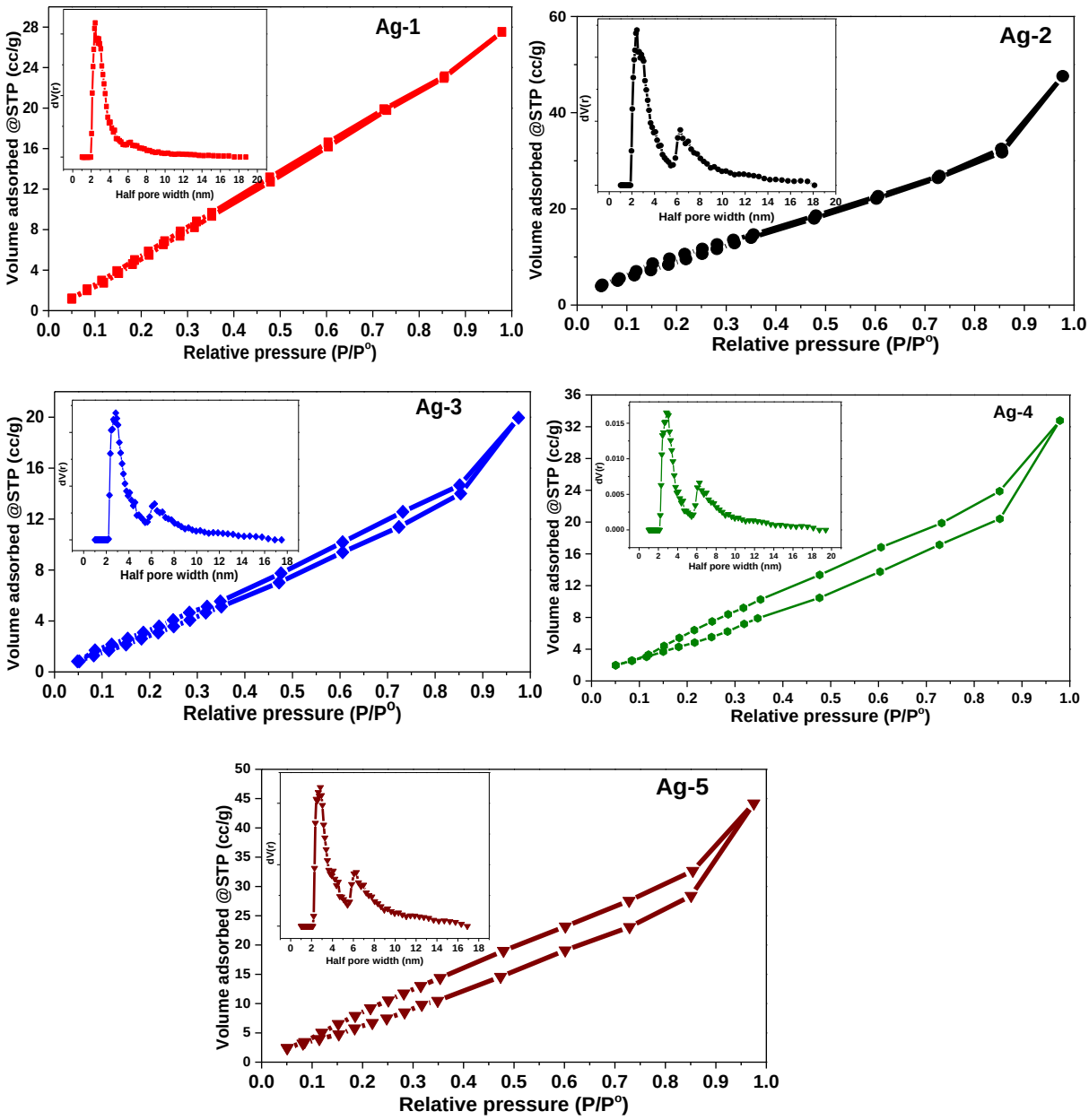

Figure 7. N_2 adsorption-desorption isotherms of synthesized Ag-based nanomaterials.

2.7. Photocatalytic Degradation of p-Nitrophenol (p-NP) over Ag Containing Nanomaterials

The photocatalytic degradation of *p*-NP aqueous solution under visible light by using synthesized silver-containing nanomaterials was performed. To study the efficacy of the synthesized catalysts, the *p*-NP degradation reaction was performed at pH 4 using 100 mL of 33 mg·L^{-1} *p*-NP solution, and 100 mg of catalyst for 120 min. As shown in Figure 8, the Ag-4 and Ag-5 samples exhibited the highest visible light photocatalytic activity than Ag-1, Ag-2, and Ag-3 samples. The degradation efficiency of Ag-1, Ag-2, and Ag-3 samples is around 2.3%, 7.1%, and 12.1%, respectively, after 20 min of reaction time, but the *p*-NP degradation efficiency of these catalysts remained constant with a further increase of reaction time. On other hand, the Ag-4 and Ag-5 samples exhibited a *p*-NP degradation efficiency of 73.28% and 48.33%, respectively. The UV-vis spectra of *p*-NP solution obtained during the photodegradation experiments are provided in the electronic Supplementary File. These results are consistent with the band gap energy of the synthesized Ag nanomaterials, as the Ag-4 sample possessed the lowest band gap energy (1.96 eV) among the synthesized samples. The photoactivity of the Ag-4 sample

is better than the Ag-5 sample. In addition to the low band gap energy, the particle size also influences the photocatalytic degradation, where the smaller particles (Ag-4 = 58 nm and Ag-5 = 75 nm) show higher photocatalytic activity because of the enhanced interfacial charge carrier transfer on the semiconductor surfaces [50].

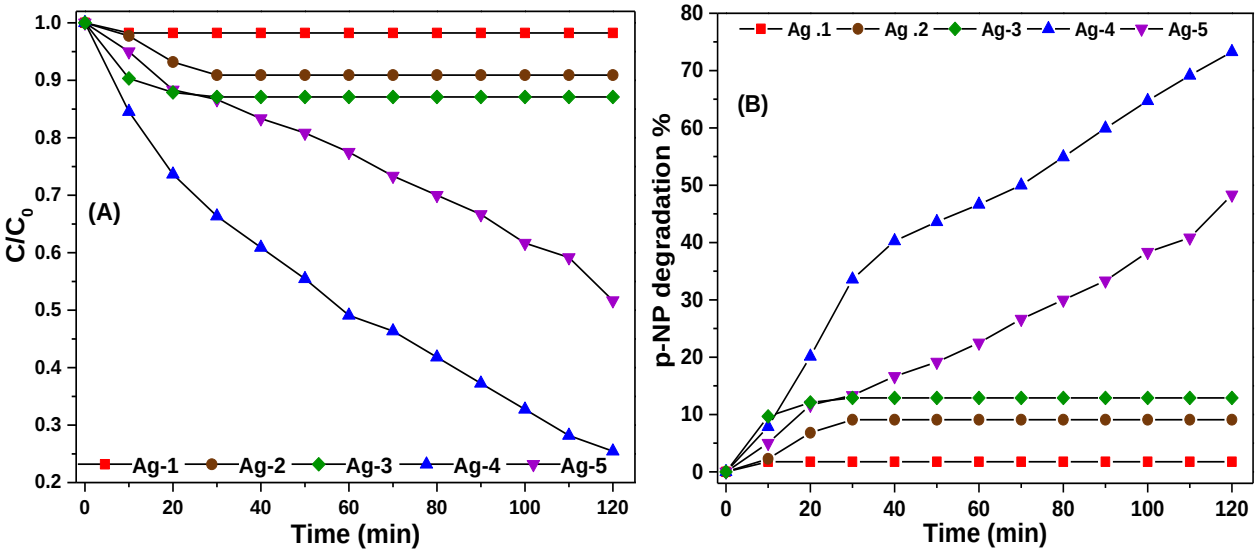

Figure 8. (**A**) Photocatalytic efficiency (**B**) percentage degradation of *p*-NP over synthesized Ag nanomaterials under visible light.

The preliminary photocatalytic activity measurements indicated that the Ag-4 sample is highly active for degradation of *p*-NP among the synthesized Ag containing nanomaterials; hence, it was chosen to study the influence of different reaction parameters under visible light. The first parameter is the pH of the *p*-NP solution; a different solution with a pH of 4, 7, and 10 were used for the experiments by keeping the reaction temperature (25 °C), mass of Ag-4 catalyst (100 mg), and *p*-NP concentration (33 mg·L^{-1}) constant. The effect of pH on *p*-NP degradation was studied by adjusting the pH with dilute HNO_3 (0.1 M) or NaOH (0.1 M) solution. The pH plays an important role in the adsorption or degradation of *p*-NP over the surface of the catalyst [51].

Figure 9A shows the *p*-NP degradation efficiency of the A*g*-4 catalyst at different pH levels, and the efficiency was increased with increase of pH of solution (from 4 to 7) and then decreased at a high pH (10) (Table 1). At pH 7, the C/C_0 is lower in the beginning of the reaction, however, *p*-NP degradation increased with time. The *p*-NP is negatively charged and the A*g*-4 catalyst could attain a negative charge under alkali conditions and electrostatic repulsions play an important role in interactions between the reactive surfaces of A*g*-4 and *p*-NP molecules. Therefore, the photodegradation is lower when the pH of the solution is high.

The second reaction parameter studied is the dose of the Ag-4 catalyst (100, 75, and 50 mg), the experiments were carried out using *p*-NP solution (concentration of 33 mg·L^{-1}; pH = 7) at 25 °C. The results obtained by changing the dose of the A*g*-4 catalyst on the degradation efficiency of *p*-NP are shown in Figure 9B and Table 2. As the catalyst dose decreased from 100 to 75 mg, the degradation efficiency of the A*g*-4 catalyst decreased slightly from 75.47% to 72.69%. Following a further decrease from 75 to 50 mg, the *p*-NP degradation efficiency of the A*g*-4 catalyst is decreased to a lower value (39.94%). An increase in degradation efficiency with an increase of catalyst dose is due to the production of photo electrons in the CB, which increases with an increase in the dose of the A*g*-4 catalyst [52]. Several *p*-NP solutions were prepared by changing the *p*-NP concentrations ranging from 16 to 33 mg·L^{-1} to investigate the influence of *p*-NP concentration on the *p*-NP degradation efficiency of the Ag-4 catalyst. Figure 9C shows the influence of the *p*-NP degradation efficiency with reaction time. With an increase of *p*-NP concentration,

the degradation efficiency of the A*g*-4 catalyst decreased (Table 2), and this is probably due to fact that more catalytically active centers are available when the *p*-NP concentration is low [53], hence, photocatalytic efficiency is increased with a decrease of *p*-NP concentration.

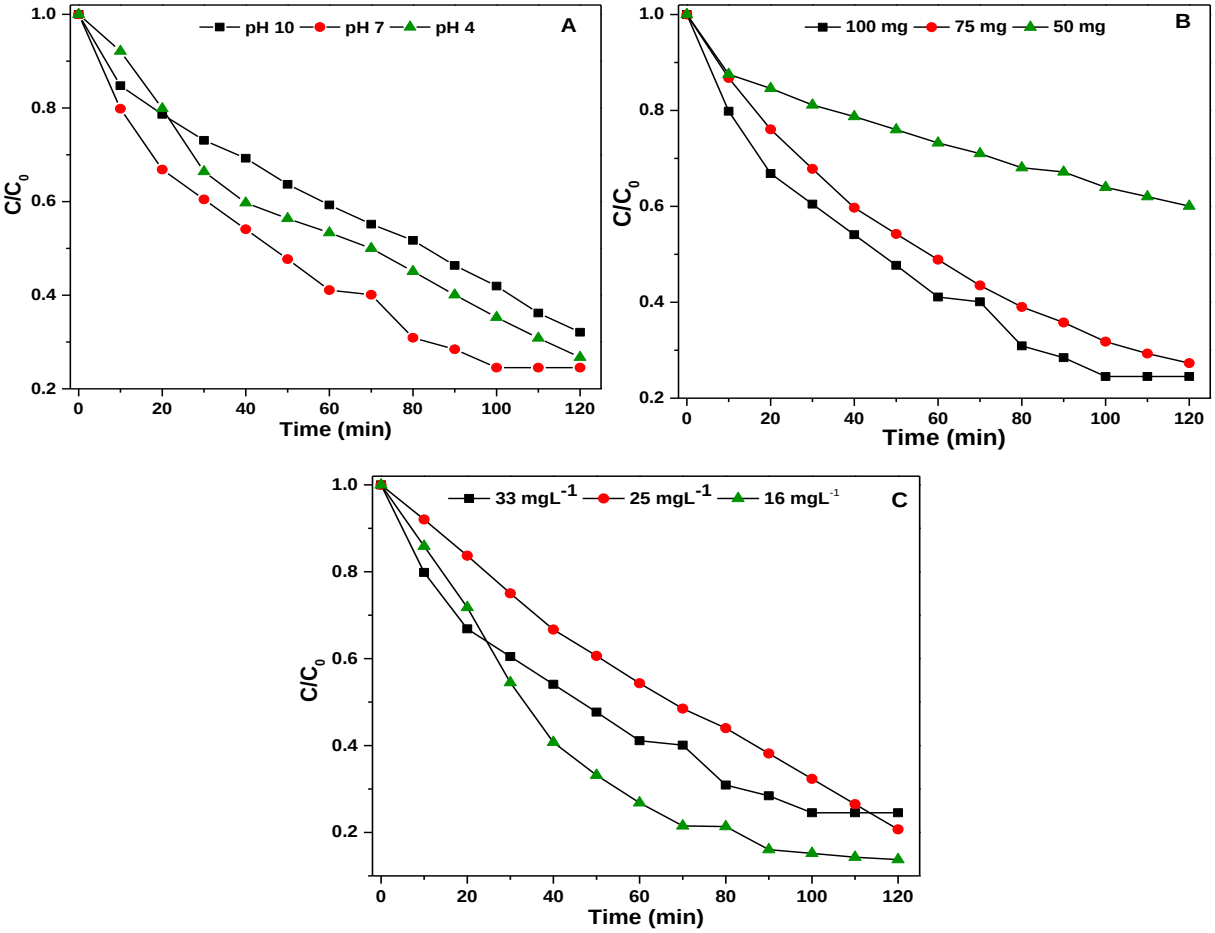

Figure 9. (**A**) Effect of pH on degradation of *p*-NP on Ag-4 catalyst under visible light, (**B**) Effect of dose of Ag-4 catalyst on degradation of $p-$NP under visible light, (**C**) Effect of $p-$NP concentration on Ag-4 catalyst degradation efficiency under visible light.

Table 2. Degradation efficiency, correlation coefficients (R), and rate constants (K) of *p*-NP degradation at different parameters.

Reaction Parameters		R^2	K (k/min^{-1})	Photodegradation Efficiency (%)
pH	10.0	0.99	0.00862	67.91
	7.0	0.98	0.01203	75.47
	4.0	0.99	0.01036	73.28
Catalyst Dose	100 mg	0.98	0.01203	75.47
	75 mg	0.99	0.01082	72.69
	50 mg	0.99	0.00375	39.94
***p*-NP Concentration**	33 mg·L^{-1}	0.98	0.01203	75.47
	25 mg·L^{-1}	0.98	0.01240	80.14
	16 mg·L^{-1}	0.98	0.01785	86.24

The *p*-NP degradation over the A*g*-4 catalyst at different reaction parameters such as pH, concentration of *p*-NP, and the dose of catalyst was well-fitted with the pseudo-first-order reaction (Equation (9));

$$\ln\frac{C_0}{C} = Kt \quad (9)$$

where '*K*' is the rate constant, '*C*' is the *p*-NP concentration solution at sampling time, and 'C_0' is initial concentration. In all cases, the values of R^2 (correlation coefficient) are higher than 0.98, which confirm the proposed kinetics for *p*-NP degradation at investigated reaction conditions and follows pseudo-first-order reaction kinetics as shown in Figure 10. The values of R^2 and k at different parameters are listed in Table 2 and the k value increases with the decreasing of *p*-NP concentration from 33 to 16 mg·L^{-1}. In addition, the value of K decreases with the decrease of a dose of A*g*-4 catalyst and increases when the pH value was increased from 4 to 7 and decreased with a further increase to 10.

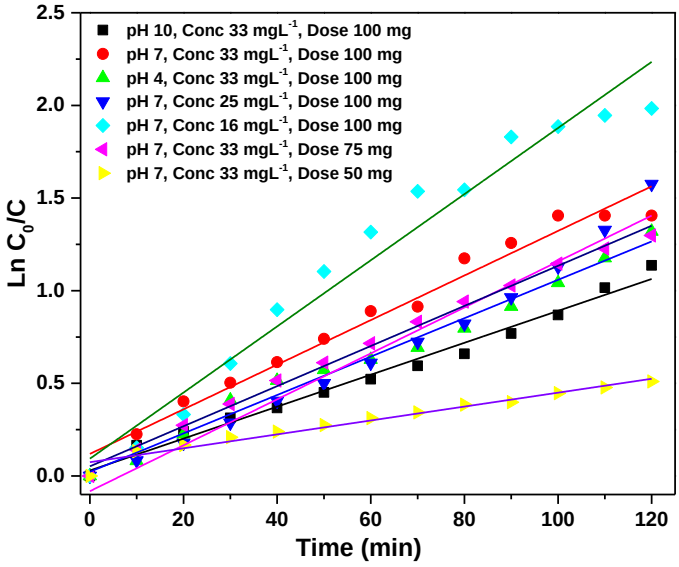

Figure 10. Derivation of the pseudo-first-order rate constants of Ag-4 catalyst at different parameters (pH, p-NP conc., Ag-4 catalyst dose) under visible light by linear regression.

The possible reaction mechanism of *p*-NP degradation over synthesized Ag-containing nanomaterials could be explained based on the physicochemical characterization results. The transition of photo electrons from VB to CB could occur in silver carbonate semiconductors under visible light irradiation. The photogenerated electrons could reduce Ag species and the reduced Ag species on the surface can be re-oxidized through the reaction with oxygen to generate superoxide radical ($\cdot O_2^-$). The $\cdot O_2^-$ radical can react with H_2O molecules to form ·OH radicals [52]. The generated ·OH and $\cdot O_2^-$ radicals are active species to degrade *p*-NP molecules under visible light.

3. Methodology

3.1. Materials

The chemicals used for current work are silver nitrate $AgNO_3$ (> 99.8%, Chem-Lab), sodium bicarbonate $NaHCO_3$ (99%, BDH Laboratory Chemicals Ltd., Poole, UK), polyvinylpyrrolidone PVP-K36, methanol (BDH Laboratory Chemicals Ltd.), ethanol (>99%, Fisher Chemical), *p*-nitrophenol (Koch-light Laboratory, Haverhill, UK), and deionized water. The chemicals were used as received.

3.2. Synthesis of Ag Containing Nanomaterials

Different synthesis conditions which were used in the preparation of Ag-based nanomaterials are tabulated in Table 3. The Ag-1 sample was prepared by using template-assisted solvothermal synthesis method. Typically, $AgNO_3$ solution (50 mL, 0.5 M) was mixed with PVP-K36 by magnetic stirring to form a clear solution. Then, $NaHCO_3$ solution (50 mL, 0.25 M) was added dropwise to the previous solution with stirring. After the dropping finished, it was stirred for 2 h. The precipitate was introduced into an autoclave and heated at 100 °C for 24 h. After that, the sample was washed three times with deionized

water and ethanol by centrifuge, then dried at 50 °C overnight and named. The Ag-2 sample was prepared using the above method, except it was not subjected to solvothermal treatment and the precipitate was washed three times with deionized water and ethanol by centrifuge directly after stirring, then dried at 50 °C overnight. Finally, both samples were calcined at 400 °C for 4 h at a heating rate of 2 °C/min.

Table 3. Different synthesis conditions adapted to prepare silver containing nanomaterials.

Sample	Synthesis Conditions				
	Template	Solvent	pH (by $NaHCO_3$)	Hydrothermal Treatment	Calcination Temp. (°C)
Ag-1	PVP-K36	MeOH:EtOH: H_2O	8	100 °C, 24 h	400
Ag-2	PVP-K36	MeOH:EtOH: H_2O	8	—	400
Ag-3	—	MeOH:EtOH: H_2O	8	—	250
Ag-4	—	MeOH:EtOH: H_2O	8	—	50
Ag-5	—	MeOH:EtOH: H_2O	8	100 °C, 24 h	50

The Ag-3 sample was prepared by the following method; initially, 4.24 g of $AgNO_3$ was dissolved in 10 mL of deionized water and 50 mL of ethanol. To this solution, a solution containing 1.05 g of $NaHCO_3$ in 25 mL of deionized water and 25 mL of methanol was added dropwise with vigorous stirring. The stirring was continued for 2 h, and then the obtained precipitate was washed three times with deionized water and ethanol. The sample was separated by centrifugation, and it was dried at 90 °C for 12 h. Finally, it was calcined at 250 °C under air for 2 h at heating rate of 2 °C/min. The Ag-4 sample was prepared by subjecting the Ag-3 sample thermal treatment at 50 °C under ambient conditions. The Ag-5 sample was prepared by following the same procedure as Ag-3 except the sample was prepared by subjecting the Ag-3 sample to solvothermal treatment at 100 °C for 24 h. The obtained product was washed three times with deionized water and ethanol and separated by centrifugation. Finally, it was dried at 50 °C for 12 h.

3.3. Photocatalytic Evaluation

Photodegradation experiments were performed with a photocatalytic reactor system. Different concentrations of *p*-nitro phenol (*p*-NP) (50 mL) and different doses of photocatalyst (g/L) were used to optimize the reaction conditions. Initially, the *p*-NP aqueous solution was magnetically stirred for 60 min in the dark to establish the adsorption–desorption equilibrium between *p*-NP and the surface of the photocatalysts. Then, the solutions were exposed to visible light irradiation under stirring using a mercury lamp (Philips, 90 W). Around 2.5 mL of *p*-NP sample was collected every 10 min by using a syringe with a filter (0.45 μm) to remove the photocatalyst particles. Then, the collected sample was analyzed using an Evolution 220 UV-*vis* spectrophotometer to record the maximum absorbance of *p*-NP solution. The efficiency of degradation was calculated using (Equation (10));

$$Degredation\ efficiency\ \% = \frac{C_0 - C}{C_0} \times 100 \quad (10)$$

where 'C_0' is initial *p*-NP concentration, and the '*C*' is final *p*-NP concentration at sampling time.

3.4. Characterization

The X-ray diffraction (XRD) patterns were recorded using a (Bruker D8 advance, Karlsruhe, Germany) diffractometer with CuKα radiation (λ = 1.54059 Å) and the experiments were performed from 5 to 80° at 2θ values and all diffraction patterns of silver materials were compared with patterns from the JCPDS database. For Fourier transform infrared spectroscopy (FT-IR) analysis, the sample was mixed with KBr and pressed in the form of a disc with a thickness of 1 mm and the analysis was carried by scanning the sample

through a wave number range of 4000 to 400 cm^{-1} using a PerkinElmer FT-IR Spectrometer (Waltham, MA, USA). A scanning electron microscopy (SEM) was used to study the morphology of the surface using a field emission scanning electron microscopy (JEOL JSM-7500 F microscope, FESEM, Tokyo, Japan). The diffuse reflectance UV-*vis* spectra (DR UV-*vis*) were obtained using a Thermo UV-*vis* spectrophotometer, Waltham, MA, USA. The specific surface area (SA_{BET}) was measured by applying the Brunauer-Emmett-Teller (BET) equation from a nitrogen adsorption-desorption isotherm using a (NOVA touch Win™ version 1.2, Quantachrome Instrument, Boynton Beach, FL, USA). X-ray photoelectron spectroscopy (XPS) measurements were performed on K-ALPHA with monochromatic X-ray Al Kα radiation from −10 to 1350 eV at pressure 10-9 mbar with spot size 400 µm at 50 eV with full spectrum pass energy 200 eV (Themo Fisher Scientific, Waltham, MA, USA).

4. Conclusions

In conclusion, silver-containing nanomaterials were synthesized by varying the synthesis conditions but using the same precursor, precipitating, and templating agents ($AgNO_3$, Na_2CO_3 and PVP etc.). Different techniques such as XRD, FT-IR, SEM, DR UV-*vis*, XPS, and N_2-physisorption were used to investigate the physicochemical properties of synthesized Ag-containing nanomaterials. Among the synthesized samples, the sample composed of a pure Ag_2CO_3 phase with nanorod morphology possessed low bandgap energy and displayed superior photocatalytic efficiency for *p*-NP decomposition in comparison with other silver nanomaterials (Ag metal and Ag_2O contained) under visible light. The *p*-NP photodegradation rate for the Ag-4 catalyst is the best when the pH of the *p*-NP aqueous solution is neutral. The *p*-NP degradation rate over the Ag-4 catalyst increased with a decrease of *p*-NP concentration and decreased with a decrease of the amount of catalyst. The degradation rate could be described as pseudo-first-order over the synthesized silver-containing nanomaterials. The high photocatalytic activity of Ag-4 sample is possibly due to the presence of a pure Ag_2CO_3 crystal structure with nanorod morphology with low band gap energy of 1.96 eV and relative high surface area.

Supplementary Materials: The following supporting information can be downloaded at: https://www.mdpi.com/article/10.3390/catal12101226/s1, Figure S1: UV-vis spectra for photocatalytic degradation of *p*-NP over synthesized Ag-1 nanomaterial under visible light, Figure S2: UV-vis spectra for photocatalytic degradation of *p*-NP over synthesized Ag-2 nano-material under visible light, Figure S3: UV-vis spectra for photocatalytic degradation of *p*-NP over synthesized Ag-3 nano-material under visible light, Figure S4: UV-vis spectra for photocatalytic degradation of *p*-NP over synthesized Ag-4 nano-material under visible light, Figure S5: UV-vis spectra for photocatalytic degradation of *p*-NP over synthesized Ag-5 nano-material under visible light.

Author Contributions: Data curation, S.D.A.-M.; formal analysis, A.A.; investigation, R.H.A.-A.; methodology, R.H.A.-A.; project administration, A.A. and K.N.; resources, K.N.; supervision, K.N.; writing–original draft, S.D.A.-M.; writing–review & editing, K.N. All authors have read and agreed to the published version of the manuscript.

Funding: Deanship of Scientific Research (DSR) at King Abdulaziz University, Jeddah, under grant no. KEP-PhD-67-130-42.

Data Availability Statement: The data presented in this study is available in Supplementary Material.

Acknowledgments: This project was funded by the Deanship of Scientific Research (DSR) at King Abdulaziz University, Jeddah, under grant no. KEP-PhD-67-130-42. The authors, therefore, acknowledge with thanks DSR for technical and financial support.

Conflicts of Interest: The authors claim that they do not have any known conflicting financial interests or personal affiliations that may seem to have impacted the work presented in this study.

References

1. Tiwari, D.K.; Behari, J.; Sen, P. Application of nanoparticles in waste water treatment. *World Appl. Sci. J.* **2008**, *3*, 417–433.
2. Pandit, M.; Paudel, K.P. Water pollution and income relationships: A seemingly unrelated partially linear analysis. *Water Resour. Res.* **2016**, *52*, 7668–7689. [CrossRef]
3. Metcalf, L.; Eddy, H.P.; Tchobanoglous, G. *Wastewater Engineering: Treatment, Disposal, and Reuse*; McGraw-Hill: New York, NY, USA, 1991; Volume 4.
4. Sonune, A.; Ghate, R. Developments in wastewater treatment methods. *Desalination* **2004**, *167*, 55–63. [CrossRef]
5. Wasewar, K.L.; Singh, S.; Kansal, S.K. Process intensification of treatment of inorganic water pollutants. *Inorg. Pollut. Water* **2020**, *13*, 245–271. [CrossRef]
6. Awaleh, M.O.; Soubaneh, Y.D. Waste Water Treatment in Chemical Industries: The Concept and Current Technologies. *Hydrol. Curr. Res.* **2014**, *5*, 1–13. [CrossRef]
7. Eichenbaum, G.; Johnson, M.; Kirkland, D.; O'Neill, P.; Stellar, S.; Bielawne, J.; DeWire, R.; Areia, D.; Bryant, S.; Weiner, S.; et al. Assessment of the genotoxic and carcinogenic risks of *p*-nitrophenol when it is present as an impu-rity in a drug product. *Regul. Toxicol. Pharmacol.* **2009**, *55*, 33–42. [CrossRef]
8. Silva, E.F.; Varela, A.S.; Cardoso, T.F.; Stefanello, F.M.; Kalb, A.C.; Martínez, P.E.; Corcini, C.D. Reproductive toxicology of 2,4 dinitrophenol in boar sperm. *Toxicol. Vitr.* **2016**, *35*, 31–35. [CrossRef]
9. Ren, Y.; Li, J.; Yuan, D.; Lai, B. Removal of *p*-nitrophenol in aqueous solution by mixed Fe^0/(passivated Fe^0) fixed bed filters. *Ind. Eng. Chem. Res.* **2017**, *56*, 9293–9302. [CrossRef]
10. Sun, S.-P.; Lemley, A.T. p-Nitrophenol degradation by a heterogeneous Fenton-like reaction on nano-magnetite: Process optimization, kinetics, and degradation pathways. *J. Mol. Catal. A Chem.* **2011**, *349*, 71–79. [CrossRef]
11. Zhang, A.; Wang, N.; Zhou, J.; Jiang, P.; Liu, G. Heterogeneous Fenton-like catalytic removal of *p*-nitrophenol in water using acid-activated fly ash. *J. Hazard. Mater.* **2012**, *201–202*, 68–73. [CrossRef]
12. Arora, P.K.; Srivastava, A.; Singh, V.P. Bacterial degradation of nitrophenols and their derivatives. *J. Hazard. Mater.* **2014**, *266*, 42–59. [CrossRef] [PubMed]
13. El Mhammedi, M.; Achak, M.; Bakasse, M.; Chtaini, A. Electrochemical determination of para-nitrophenol at apatite-modified carbon paste electrode: Application in river water samples. *J. Hazard. Mater.* **2009**, *163*, 323–328. [CrossRef] [PubMed]
14. Mei, Q.; Cao, H.; Han, D.; Li, M.; Yao, S.; Xie, J.; Zhan, J.; Zhang, Q.; Wang, W.; He, M.; et al. Theoretical insight into the degradation of *p*-nitrophenol by OH radicals synergized with other active oxidants in aqueous solution. *J. Hazard. Mater.* **2020**, *389*, 121901. [CrossRef]
15. Kuo, W. Decolorizing dye wastewater with Fenton's reagent. *Water Res.* **1992**, *26*, 881–886. [CrossRef]
16. Padmanabhan, P.; Sreekumar, K.; Thiyagarajan, T.; Satpute, R.; Bhanumurthy, K.; Sengupta, P.; Dey, G.; Warrier, K. Nanocrystalline titanium dioxide formed by reactive plasma synthesis. *Vacuum* **2006**, *80*, 1252–1255. [CrossRef]
17. Gaya, U.I.; Abdullah, A.H. Heterogeneous photocatalytic degradation of organic contaminants over titanium dioxide: A review of fundamentals, progress and problems. *J. Photochem. Photobiol. C Photochem. Rev.* **2008**, *9*, 1–12. [CrossRef]
18. Yang, H.; Cheng, H. Controlling nitrite level in drinking water by chlorination and chloramination. *Sep. Purif. Technol.* **2007**, *56*, 392–396. [CrossRef]
19. Lu, J.; Zhang, T.; Ma, J.; Chen, Z. Evaluation of disinfection by-products formation during chlorination and chloramination of dissolved natural organic matter fractions isolated from a filtered river water. *J. Hazard. Mater.* **2009**, *162*, 140–145. [CrossRef]
20. An, C.; Wang, S.; Sun, Y.; Zhang, Q.; Zhang, J.; Wang, C.; Fang, J. Plasmonic silver incorporated silver halides for efficient photocatalysis. *J. Mater. Chem. A* **2015**, *4*, 4336–4352. [CrossRef]
21. Li, L.; Gao, H.; Liu, G.; Wang, S.; Yi, Z.; Wu, X.; Yang, H. Synthesis of carnation flower-like $Bi_2O_2CO_3$ photocatalyst and its promising application for photoreduction of Cr(VI). *Adv. Powder Technol.* **2022**, *33*, 103481. [CrossRef]
22. Li, L.; Gao, H.; Yi, Z.; Wang, S.; Wu, X.; Li, R.; Yang, H. Comparative investigation on synthesis, morphological tailoring and photocatalytic activities $Bi_2O_2CO_3$ nanostructures. *Colloids Surf. A Physicochem. Eng. Asp.* **2022**, *644*, 128758. [CrossRef]
23. Yu, H.; Chen, W.; Wang, X.; Xu, Y.; Yu, J. Enhanced photocatalytic activity and photoinduced stability of Ag-based photocatalysts: The synergistic action of amorphous-Ti(IV) and Fe(III) cocatalysts. *Appl. Catal. B Environ.* **2016**, *187*, 163–170. [CrossRef]
24. Shi, J.; Ye, J.; Li, Q.; Zhou, Z.; Tong, H.; Xi, G.; Guo, L. Single-Crystal Nanosheet-Based Hierarchical $AgSbO_3$ with Exposed {001} Facets: Topotactic Synthesis and En-hanced Photocatalytic Activity. *Chem. A Eur. J.* **2012**, *18*, 3157–3162. [CrossRef]
25. Dai, G.; Yu, J.; Liu, G. A new approach for photocorrosion inhibition of Ag_2CO_3 photocatalyst with highly visi-ble-light-responsive reactivity. *J. Phys. Chem. C* **2012**, *116*, 15519–15524. [CrossRef]
26. Ao, Y.; Wang, P.; Wang, C.; Hou, J.; Qian, J. Preparation of graphene oxide-Ag_3PO_4 composite photocatalyst with high visible light photocatalytic activity. *Appl. Surf. Sci.* **2013**, *271*, 265–270. [CrossRef]
27. Wang, X.; Li, S.; Ma, Y.; Yu, H.; Yu, J. $H_2WO_4{\cdot}H_2O$/Ag/AgCl composite nanoplates: A plasmonic Z-scheme visible-light photocatalyst. *J. Phys. Chem. C* **2011**, *115*, 14648–14655. [CrossRef]
28. Xu, H.; Li, H.; Xu, L.; Wu, C.; Sun, G.; Xu, Y.; Chu, J. Enhanced Photocatalytic Activity of Ag_3VO_4 Loaded with Rare-Earth Elements under Visible-Light Irradiation. *Ind. Eng. Chem. Res.* **2009**, *48*, 10771–10778. [CrossRef]
29. Wang, X.; Li, S.; Yu, H.; Yu, J.; Liu, S. Ag_2O as a new visible-light photocatalyst: Self-stability and high photocatalytic activity. *Chem. A Eur. J.* **2011**, *17*, 7777–7780. [CrossRef]

30. Schrand, A.M.; Rahman, M.F.; Hussain, S.M.; Schlager, J.J.; Smith, D.A.; Syed, A.F. Metal-based nanoparticles and their toxicity assessment. *Wiley Interdiscip. Rev. Nanomed. Nanobiotechnology* **2010**, *2*, 544–568. [CrossRef] [PubMed]
31. Yin, L.-S.; Yang, S.-Y.; He, X.; Fan, H.-L. New Preparation Method and Characterization of Spheric Silver Nanoparticles. *Nanotechnol. Precis. Eng.* **2010**, *8*, 295–299.
32. Zhang, Z.; Zhao, B.; Hu, L. PVP Protective Mechanism of Ultrafine Silver Powder Synthesized by Chemical Reduction Processes. *J. Solid State Chem.* **1996**, *121*, 105–110. [CrossRef]
33. Lu, H. Fabrication and characterization of porous silver powder prepared by spray drying and calcining technology. *Powder Technol.* **2010**, *203*, 176–179. [CrossRef]
34. Yu, C.; Li, G.; Kumar, S.; Yang, K.; Jin, R. ChemInform Abstract: Phase Transformation Synthesis of Novel Ag_2O/Ag_2CO_3 Heterostructures with High Visible Light Efficiency in Photocatalytic Degradation of Pollutants. *Adv. Mater.* **2014**, *26*, 892–898. [CrossRef] [PubMed]
35. García, J.; López, T.; Álvarez, M.; Aguilar, D.H.; Quintana, P. Spectroscopic, structural and textural properties of CaO and $CaO-SiO_2$ materials synthesized by sol–gel with different acid catalysts. *J. Non-Cryst. Solids* **2008**, *354*, 729–732. [CrossRef]
36. Xu, H.; Song, Y.; Song, Y.; Zhu, J.; Zhu, T.; Liu, C.; Zhao, D.; Zhang, Q.; Li, H. Synthesis and characterization of $g\text{-}C_3N_4/Ag_2CO_3$ with enhanced visible-light photocatalytic activity for the degradation of organic pollutants. *RSC Adv.* **2014**, *4*, 34539–34547. [CrossRef]
37. Sohrabnezhad, S.; Pourahmad, A.; Moghaddam, M.J.M.; Sadeghi, A. Study of antibacterial activity of Ag and Ag_2CO_3 nanoparticles stabilized over montmorillonite. *Spectrochim. Acta Part A Mol. Biomol. Spectrosc.* **2015**, *136*, 1728–1733. [CrossRef]
38. Kumar, M.R.; Murugadoss, G.; Venkatesh, N.; Sakthivel, P. Synthesis of Ag_2O-SnO_2 and SnO_2-Ag_2O Nanocomposites and Investigation on Photocatalytic Perfor-mance under Direct Sun Light. *ChemistrySelect* **2020**, *5*, 6946–6953. [CrossRef]
39. Sharma, V.; Verma, D.; Okram, G.S. Influence of surfactant, particle size and dispersion medium on surface plasmon resonance of silver nanoparticles. *J. Phys. Condens. Matter* **2019**, *32*, 145302. [CrossRef] [PubMed]
40. Daniel, L.; Nagai, H.; Sato, M. Photoelectrochemical property and the mechanism of plasmonic Ag-NP/TiO_2 composite thin films with high silver content fabricated using molecular precursor method. *J. Mater. Sci.* **2013**, *3*, 625–645.
41. Fakhri, M.A. Annealing effects on opto-electronic properties of Ag_2O films growth using thermal evaporation techniques. *Int. J. Nanoelectron. Mater.* **2016**, *9*, 93–102.
42. Jiang, W.; Zeng, Y.; Wang, X.; Yue, X.; Yuan, S.; Lu, H.; Liang, B. Preparation of Silver Carbonate and its Application as Visible Light-driven Photocatalyst Without Sacrifi-cial Reagent. *Photochem. Photobiol.* **2015**, *91*, 1315–1323. [CrossRef] [PubMed]
43. Bazant, P.; Kuritka, I.; Munster, L.; Kalina, L. Microwave solvothermal decoration of the cellulose surface by nanostructured hybrid Ag/ZnO particles: A joint XPS, XRD and SEM study. *Cellulose* **2015**, *22*, 1275–1293. [CrossRef]
44. Kumar-Krishnan, S.; Prokhorov, E.; Hernández-Iturriaga, M.; Mota-Morales, J.D.; Vázquez-Lepe, M.; Kovalenko, Y. Chitosan/silver nanocomposites: Synergistic antibacterial action of silver nanoparticles and sil-ver ions. *Eur. Polym. J.* **2015**, *67*, 242–251. [CrossRef]
45. Wang, H.; Li, J.; Huo, P.; Yan, Y.; Guan, Q. Preparation of Ag_2O/Ag_2CO_3/MWNTs composite photocatalysts for enhancement of ciprofloxacin degrada-tion. *Appl. Surf. Sci.* **2016**, *366*, 1–8. [CrossRef]
46. Fang, D.; He, F.; Xie, J.; Xue, L. Calibration of Binding Energy Positions with C1s for XPS Results. *J. Wuhan Univ. Technol. Sci. Ed.* **2020**, *35*, 711–718. [CrossRef]
47. Gillen, A.J.; Villevieille, C.; Berg, E.J.; Novák, P.; El Kazzi, M. *Investigation of the Early Stages of Surface Layer Formation on Cycled HE-NCM vs. LTO Electrodes Using XPS*; PSI Electrochemistry Laboratory-Annual Report; Paul Scherrer Institut (PSI): Villigen, Switzerland, 2011; p. 63.
48. Shi, L.; Liang, L.; Wang, F.; Liu, M.; Sun, J. Enhanced visible-light photocatalytic activity and stability over $g\text{-}C_3N_4/Ag_2CO_3$ composites. *J. Mater. Sci.* **2015**, *50*, 1718–1727. [CrossRef]
49. Ladavos, A.; Katsoulidis, A.; Iosifidis, A.; Triantafyllidis, K.; Pinnavaia, T.; Pomonis, P. The BET equation, the inflection points of N_2 adsorption isotherms and the estimation of specific surface area of porous solids. *Microporous Mesoporous Mater.* **2011**, *151*, 126–133. [CrossRef]
50. Lee, S.-Y.; Park, S.-J. TiO_2 photocatalyst for water treatment applications. *J. Ind. Eng. Chem.* **2013**, *19*, 1761–1769. [CrossRef]
51. Długosz, O.; Szostak, K.; Krupiński, M.; Banach, M. Synthesis of Fe_3O_4/ZnO nanoparticles and their application for the photodegradation of anionic and cat-ionic dyes. *Int. J. Environ. Sci. Technol.* **2021**, *18*, 561–574. [CrossRef]
52. Dai, K.; Lu, L.; Dawson, G. Development of UV-LED/TiO_2 device and their application for photocatalytic degradation of methylene blue. *J. Mater. Eng. Perform.* **2013**, *22*, 1035–1040. [CrossRef]
53. Dariani, R.; Esmaeili, A.; Mortezaali, A.; Dehghanpour, S. Photocatalytic reaction and degradation of methylene blue on TiO_2 nano-sized particles. *Optik* **2016**, *127*, 7143–7154. [CrossRef]